FOCUS: MS/MS PEPTIDE IDENTIFICATION: RESEARCH ARTICLE

Thermodynamics and Mechanisms of Protonated Diglycine Decomposition: A Guided Ion Beam Study

P. B. Armentrout, Amy L. Heaton

Department of Chemistry, University of Utah, Salt Lake City, UT 84112, USA

Abstract

We present a full molecular description of fragmentation reactions of protonated diglycine (H^+GG) by studying their collision-induced dissociation (CID) with Xe using a guided ion beam tandem mass spectrometer (GIBMS). Analysis of the kinetic energy-dependent CID cross sections provides the 0 K barriers for the sequential H_2O+CO and $CO+NH_3$ losses from H^+GG as well as for the reactions involved in y_1 and a_1 ion formation, after accounting for unimolecular decay rates, internal energy of reactant ions, and multiple ion-molecule collisions. Here, seven energetic barriers are measured for the fragmentation processes of H^+GG, including the loss of H_2O and of CO at ~140 and ~156 kJ/mol, the combined loss of (H_2O+CO) and of ($CO+NH_3$) at ~233 and ~185 kJ/mol, and formation of y_1 and a_1 ions at ~191 and ~212 kJ/mol, respectively, with a second channel for a_1 formation opening at ~326 kJ/mol. Theoretical energies from the preceding paper are compared with our experimental energies and found to be in good agreement. This validates the mechanisms explored computationally, including unambiguous identification of the b_2 ion as protonated 2-aminomethyl-5-oxazolone, thereby allowing a complete characterization of the elementary steps of H^+GG decomposition. These results also demonstrate that all reactive species are available from the ground state conformation, as opposed to involving an initial broad distribution of protonated conformers. This result verifies the utility of the "mobile proton" model for understanding the fragmentation of protonated proteins.

Key words: Diglycine, Energetics, Protonated peptides, Mechanism, Mobile proton

Introduction

The gas phase fragmentation of protonated peptides often occurs at the peptide linkages, producing b ions when the charge is retained on the N-terminal fragment and y ions when the C-terminal fragment carries the charge. Other common fragmentations include the loss of CH_2O_2. Despite the importance of such decompositions in understanding gas-phase reactivity of biologically relevant peptides and the ability of mass spectrometry to provide detailed sequence information, quantitative experimental characterizations of such processes are limited [1–5]. In an early pioneering study, Klassen and Kebarle [2] measured the dominant, low-energy CID fragment ions of protonated G_n ($n=1–4$) and several related compounds using a modified triple quadrupole mass spectrometer. Reid, Simpson, and O'Hair, as well as Wesdemiotis and coworkers, have examined the qualitative breakdown diagram of protonated

diglycine, H^+GG, as a function of collision energy, although no quantitative information was experimentally acquired [6–8]. In the most complete study to date, Siu and coworkers examined the threshold collision-induced dissociation of protonated GGG, AGG, and GAG and extracted threshold energy information that compares well with theory [3, 9]. Recently, we completed a similar study of the simplest system of this type, protonated glycine, H^+G [10]. These latter studies illustrate the utility of having good quantitative thermodynamic information available to confirm theoretical studies of mechanisms.

Here, we comprehensively characterize the fragmentation reactions of H^+GG by using gas-phase threshold collision-induced dissociation (TCID) experiments carried out in a guided ion beam tandem mass spectrometer (GIBMS). We measure absolute experimental energetics for the observed reactions utilizing calculations from the preceding paper (paper I) [11] to provide structures, vibrational frequencies, and rotational constants needed for accurate analysis. Experimental threshold energies are compared with theoretical single point energy calculations at both B3LYP and MP2 levels from paper I in order to fully characterize the key steps of H^+GG decomposition. Overall, the agreement between the experimental thermochemistry determined here and that calculated is found to be reasonable.

An important finding in the present results is that the multitude of products ordinarily observed in the fragmentation of these protonated systems are available from the ground state conformer, i.e., a broad distribution of different protonation sites are formed upon collisional excitation of the ground state conformer. Importantly, this observation is fully consistent with the "mobile proton" model [12], a key concept in understanding the fragmentation of protonated proteins.

Experimental

General Experimental Procedures

Cross sections for CID of protonated diglycine are measured using a GIBMS that has been described in detail previously [13, 14]. Experiments are conducted using an electrospray ionization (ESI) source [15] under conditions similar to those described previously [15–18]. Briefly, the ESI is operated using either H_2O or 50:50 by volume $H_2O/MeOH$ solutions with ~10^{-4} M diglycine (all chemicals purchased from Sigma-Aldrich), syringe-pumped at a rate of 0.04 mL/hr into a 35 gauge stainless steel needle biased at ~2000 V. Ionization occurs over the ~5 mm distance from the tip of the needle to the entrance of the capillary, biased at ~35 V. Ions are directed by a capillary heated to 80 °C into a radio frequency (rf) ion funnel [19], wherein they are focused into a tight beam. Ions exit the ion funnel and enter an rf hexapole ion guide that traps them radially. Here the ions undergo multiple collisions (>10^4) with the ambient gas and become thermalized. Ions produced in the source are assumed to have their internal energies well described by a Maxwell-Boltzmann distribution of rovibrational states at 300 K, as characterized in previous experiments [15, 17, 18, 20].

Ions are extracted from the source, mass selected using a magnetic momentum analyzer, decelerated to a well-defined kinetic energy, and focused into a rf octopole ion guide that traps the ions radially [21, 22]. The ion guide minimizes losses of the reactant and any product ions resulting from scattering. The octopole passes through a static gas cell containing xenon, which is used as the collision gas for reasons described elsewhere [23, 24]. After collision, the reactant and product ions drift to the end of the octopole where they are extracted and focused into a quadrupole mass filter for mass analysis. The ions are detected with a high voltage dynode, scintillation ion detector [25], and the signal is processed using standard pulse counting techniques. Ion intensities, measured as a function of collision energy, are converted to absolute cross sections as described previously [13]. The uncertainty in relative cross sections is about ±5% and that for the absolute cross sections is about ±20%. The ion kinetic energy distribution is measured to be Gaussian and has a typical full width at half maximum (FWHM) of 0.1−0.2 eV (lab). Uncertainties in the absolute energy scale are about ±0.05 eV (lab). Ion kinetic energies in the laboratory frame are converted to energies in the center-of-mass (CM) frame using $E_{CM}=E_{lab} \, m/(m+M)$, where M and m are the masses of the ionic and neutral reactants, respectively. All energies herein are reported in the CM frame unless otherwise noted.

Thermochemical Analysis

Threshold regions of the CID reaction cross sections are modeled using Equation 1,

$$\sigma_j(E) = (n\sigma_{0,j}/E) \sum_i g_i \int_{E_{0,j}-E_i}^{E} [k_j(E*)/k_{tot}(E*)](E - \varepsilon)^{n-1} P_{D1} d(\varepsilon)$$

(1)

where $\sigma_{0,j}$ is an energy-independent scaling factor for channel j, n is an adjustable parameter that describes the efficiency of collisional energy transfer [14], E is the relative kinetic energy of the reactants, $E_{0,j}$ is the threshold energy for CID of the ground electronic and rovibrational state of the reactant ion at 0 K for channel j, ε is the energy transferred from translation during the collision, and $E*$ is the internal energy of the energized molecule (EM) after the collision, i.e., $E* = \varepsilon + E_i$. The term $k_j(E*)$ is the unimolecular rate coefficient for dissociation of the EM to channel j, and its summation over all channels yields $k_{tot}(E*)$. P_{D1} is the probability for dissociation of the EM and is given by $1 - \exp[-k_{tot}(E*)\tau]$, where τ is the experimental time for dissociation (~5×10^{-4} s in the extended dual octopole configuration as measured by time-of-flight studies) [14]. The summation in Equation 1 is over

the rovibrational states of the reactant ions, i, where E_i is the excitation energy of each state and g_i is the fractional population of those states ($\Sigma g_i = 1$). This equation accounts for the lifetime for dissociation of the EM, which can lead to a delayed onset for the reaction threshold, a kinetic shift, which becomes more noticeable as the size of the EM increases. In addition, Equation 1 naturally includes competition among parallel reactions with a full statistical treatment [26]. Previous studies have verified the efficacy of this approach in modeling reactions that compete through loose as well as loose versus tight transition states [10, 14, 27–31].

The rate coefficients $k_j(E^*)$ necessary for competitive modeling and $k_{tot}(E^*)$ are defined by Rice-Ramsperger-Kassel-Marcus (RRKM) theory as in Equation 2 [32, 33],

$$k_{tot}(E^*) = \sum_j k_j(E^*) = \sum_j d_j N_j^{\ddagger}(E^* - E_{0,j})/h\rho(E^*) \quad (2)$$

where d_j is the reaction degeneracy of channel j (defined using ratios of the rotational constants of reactants and products), $N_j^{\ddagger}(E^* - E_{0,j})$ is the sum of rovibrational states of the transition state (TS) for channel j at an energy $E^* - E_{0,j}$, and $\rho(E^*)$ is the density of states of the EM at the available energy, E^*. Vibrational frequencies and rotational constants are taken from quantum chemical calculations as detailed in paper I. The Beyer-Swinehart-Stein-Rabinovitch algorithm [34–36] is used to evaluate the number and density of the rovibrational states, and the relative populations g_i are calculated for a Maxwell-Boltzmann distribution at 300 K. For reactions limited by loose TSs, most frequencies are those of the products with the transitional frequencies treated as rotors, an approach that corresponds to a phase space limit (PSL), as described in detail elsewhere [26, 37]. The two-dimensional (2D) external rotations are treated adiabatically but with centrifugal effects included [36], and calculated using a statistical distribution with an explicit summation over all the possible values of the rotational quantum number. For reactions limited by tight TSs, molecular parameters are taken from theoretical results.

Because the decomposition of H^+GG also involves several sequential dissociation pathways, accurate modeling of the data requires additional assumptions to describe such processes, as described previously [38]. The difficulty in analyzing sequential thresholds lies in the fact that the initial dissociation process takes away an unknown distribution of energies in translational modes of the initial products, as well as internal modes of the neutral product. This leaves an unknown distribution of internal energies in the ionic product that undergoes further dissociation. The procedure used to handle this effect uses Equation 1 to reproduce the cross section for the product of the primary reaction, which excludes subsequent dissociation, $\sigma_{CID}(E)$, combined with the probability for further dissociation, $P_{D2} = 1 - \exp\left[-k_{2tot}\left(E_2^*\right)\tau_2\right]$. Here k_{2tot},

E_2^*, and τ_2 are the total rate coefficient for the secondary dissociation, the energy available to the secondary EM, and the time available for the secondary dissociation, respectively. This partitions the total CID cross section into that for the non-dissociating products, 1, and that for the sequential dissociation product ion, 2, as described in Equation 3.

$$\sigma_1(E) = \sigma_{CID}(E)(1 - P_{D2}), \quad (3a)$$

$$\sigma_2(E) = \sigma_{CID}(E)P_{D2} \quad (3b)$$

Here, the rate coefficients are again calculated using RRKM theory, Equation 2, for the new EM. The energy available to this EM is defined statistically, accomplished by methods described in detail elsewhere [38]. In our previous work, only a single sequential channel was included in our data analysis program (CRUNCH); however, it is conceptually straightforward to include additional competitive channels (j) in the same manner as Equation 1, specifically, $k_{2tot} = \Sigma\ k_{2j}$ and $\sigma_{2j} = \sigma_2\left[k_{2j}\left(E_2^*\right)/k_{2tot}\left(E_2^*\right)\right]$. This capability has now been included and is utilized below for the first time. The combination of sequential and competitive modeling allows accurate reproduction of all experimental reaction cross sections observed here, as detailed further below.

Several effects that would otherwise obscure the interpretation of the data must also be accounted for during data analysis. The first involves energy broadening resulting from the thermal motion of the neutral collision gas and the kinetic energy distribution of the reactant ion, accounted for by explicitly convoluting the models of Equations 1 and 3a, 3b over both kinetic energy distributions [13]. The second effect considers that our models only represent products formed as the result of a single collision event, which we account for by evaluating the cross sections for pressure effects and extrapolating to zero pressure of Xe (rigorously single collision conditions) when necessary [39].

After convolution with the kinetic energy distribution of the reactants, the model cross sections of Equations 1 and 3a, 3b are compared with the data. A nonlinear least-squares analysis is used to provide optimized values for $\sigma_{0,j}$, n, and $E_{0,j}$. The uncertainty associated with $E_{0,j}$ is estimated from the range of threshold values determined from different data sets, 10% variations in the vibrational frequencies, changes in τ by factors of 2, and the uncertainty of the absolute energy scale, 0.05 eV (lab). For loose TSs, we assume that the measured threshold E_0 values for dissociation are from ground state reactant to ground state ion and neutral ligand products. Given the relatively long experimental time frame ($\sim 5 \times 10^{-4}$ s), dissociating complexes should be able to rearrange to their ground state product conformations upon dissociation.

Results

Cross Sections for Collision-Induced Dissociation

Kinetic energy dependent experimental cross sections were obtained for the interaction of H^+GG with Xe. Figure 1 shows a representative data set, which is a mean of results taken at xenon pressures of ~0.05, 0.1, and 0.2 mTorr, as very little pressure dependence was detected within our experimental uncertainties. For the H^+GG system (m/z 133), six ionic products are observed, Figure 1, consistent with reactions 4–9a, 9b.

$$H^+GG + Xe \rightarrow C_4H_7N_2O_2^+(b_2) + H_2O + Xe \qquad (4)$$

$$\rightarrow C_3H_9N_2O_2^+ + CO + Xe \qquad (5)$$

$$\rightarrow C_3H_6NO_2^+ + CO + NH_3 + Xe \qquad (6)$$

$$\rightarrow C_3H_7N_2O^+(a_2) + CO + H_2O + Xe \qquad (7)$$

$$\rightarrow C_2H_6NO_2^+(y_1, H^+G) + CO + CH_2NH + Xe \qquad (8)$$

$$\rightarrow CH_2NH_2^+(a_1) + CO + C_2H_5NO_2(G) + Xe \qquad (9a)$$

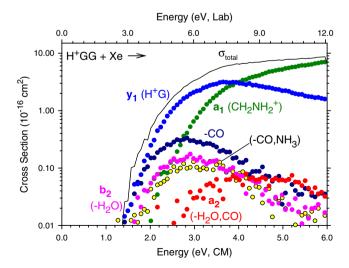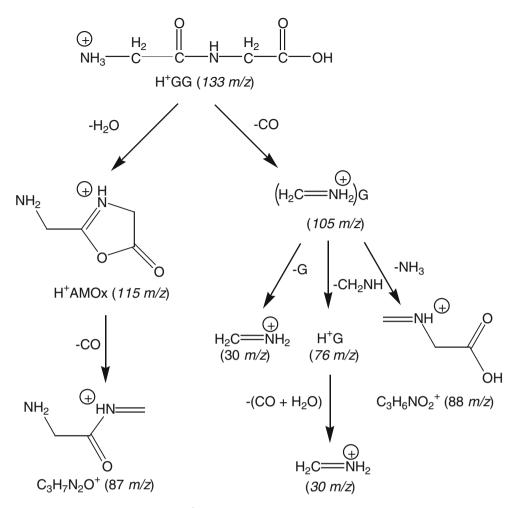$$\rightarrow CH_2NH_2^+(a_1) + H_2O + 2CO + CH_2NH + Xe \qquad (9b)$$

Figure 1. Cross sections for collision-induced dissociation of H^+GG with Xe as a function of kinetic energy in the center-of-mass frame (lower x-axis) and the laboratory frame (upper x-axis)

The lowest energy process observed is the loss of CO (m/z 105), reaction 5, followed almost immediately by formation of the y_1 ion, protonated glycine (H^+G) at m/z 76, in reaction 8. The threshold for loss of H_2O in reaction 4, forming the b_2 ion at m/z 115, is slightly higher in energy, followed shortly thereafter by the combined losses of ($CO+NH_3$) at m/z 88 in reaction 6. (We explicitly looked for loss of NH_3 alone but found no such product at m/z 116.) Formation of the a_1 ion (m/z 30) in reaction 9a has a similar apparent threshold. Loss of both CO and H_2O to form the a_2 ion (m/z 87) in reaction 7 has the highest threshold observed. The ionic products of reactions 8 (y_1) and 9 (a_1) are clearly more efficient than the reactions corresponding to loss of the small neutral molecules, reactions 4–7. Finally, it can be seen that the cross section for reaction 8 declines at higher energies, which can be attributed to the decomposition of the H^+G (y_1) product ion to form a_1 in the overall reaction 9b. This subsequent decomposition has been verified by the CID of H^+G in a previous study [10].

In contrast to the current study, Klassen and Kebarle [2] observed only the major y_1 and a_1 channels with relative intensities that exhibit qualitatively the same behavior as that shown in Figure 1. In their energy-resolved fragmentation study of H^+GG formed by electrospray ionization, Reid et al. [6] report qualitative breakdown results for only reactions 4 and 8, but list abundances for the other product ions consistent with those observed here. Wesdemiotis and coworkers examined the energy-resolved breakdown diagram for dissociation of H^+GG formed by FAB in collisions with Ar [8]. They observe the same five major product ions as found here, those from reactions 4, 5, 6, 8, and 9a, 9b, with relative energetic behavior that agrees well with the present results. However, their results are shifted to higher energies compared with those obtained here, even once the difference in the mass of the collision partner, Xe versus Ar, is accounted for. In contrast, the energetic behavior reported by Reid et al. matches that observed here once this correction has been applied.

Analysis of Cross Sections for H^+GG Decomposition—Primary Dissociation Channels

The six ionic product channels observed were modeled corresponding to reactions 4–9a, 9b described above. On the basis of the reaction coordinate surfaces calculated in paper I, Scheme 1 represents the pathways involved. Loss of H_2O and CO, reactions 4 and 5, respectively, can both occur as a primary dissociation from H^+GG and are limited by the tight transition states, $TS[N_1-O_3]$-ttgct or $TS[O_1-O_3]$-ctggt and TS $[N_2]\{C_{\alpha1}\sim OC\sim N_2\}$ (ttgtt or cggtt), respectively, rather than by the asymptotic energies of the products, Figures 1 and 3 of paper I. (See paper I for a description of the nomenclature used here to identify structures.) The b_2 product ion from reaction 4, protonated 2-aminomethyl-5-oxazolone (H^+AMOx), can further dissociate to form a_2 according to reaction

H^+GG (133 m/z)

−H₂O   −CO

H^+AMOx (115 m/z)

$(H_2C=NH_2)G$ (105 m/z)

−G   −CH₂NH   −NH₃

$H_2C=NH_2$ (30 m/z)

H^+G (76 m/z)

$C_3H_6NO_2^+$ (88 m/z)

−CO

−(CO + H₂O)

$C_3H_7N_2O^+$ (87 m/z)

$H_2C=NH_2$ (30 m/z)

Scheme 1. Schematic reaction mechanism for H^+GG decomposition

(7). The calculations indicate that if the water is lost before decomposition of the oxazolone ring, then the reactions are sequential with formation of the a_2 ion limited by the tight transition state, $TS(H^+AMOx[N_2]$-c$\{OC{\sim}O\})$, Figure 4 of paper I. However, if the oxazolone ring decomposes before the water is lost, the system passes over $TS(H^+AMOx[N_2]$-c$\{OC{\sim}O\})(H_2O_{HN2})$ and the loss of CO and H₂O is limited by the energy of the product asymptote, i.e., a loose TS, Figure 4 of paper I. The ionic product from reaction 5, $(CH_2NH_2^+)(G)$, can also dissociate further according to reactions 6, 8, and 9a, where the former passes over a tight TS, Figure 5 of paper I, and the latter two channels involve loose TSs, Figure 1 of paper I. Finally, the y_1 (H^+G) product of reaction 8 can dissociate to form the a_1 product ion in reaction 9b, as previously elucidated [10].

To model these interrelated and complex processes, the cross sections for reactions 5, 6, 8, and 9a, 9b (initial loss of CO) were summed and modeled competitively with the sum of the cross sections for reactions 4 and 7 (initial loss of H₂O) using Equation 1. This model provides the threshold energies for reactions 4 and 5, as listed in Table 1. For H₂O loss, the data were modeled using either $TS[N_1$-$O_3]$-ttgct or $TS[O_1$-$O_3]$-ctggt; and for CO loss, either $TS[N_2]$-ttgtt $\{C_{\alpha1}{\sim}OC{\sim}N_2\}$ or $TS[N_2]$-cggtt$\{C_{\alpha1}{\sim}OC{\sim}N_2\}$ were utilized. Other TSs for these processes are either higher in energy or more constrained such that they should not contribute appreciably to the observed processes. Significantly, no scaling of the individual channels was needed, i.e., statistical factors are sufficient to accurately describe the relative magnitudes of both cross sections. The data are reproduced slightly better when using the looser $TS[N_2]$-ttgtt $\{C_{\alpha1}{\sim}OC{\sim}N_2\}$ ($\Delta S^{\ddagger}=50$ J/K mol) compared with $TS[N_2]$-cggtt$\{C_{\alpha1}{\sim}OC{\sim}N_2\}$ ($\Delta S^{\ddagger}=45$ J/K mol), although the changes in threshold energies are small (≤ 0.10 eV, within the stated experimental uncertainties). (If these two TSs are given the same threshold energy, in accord with the relative energies calculated in paper I, the rate for passing over the looser ttgtt TS is 2.3 times faster than for passing over the cggtt TS. Thus, the ttgtt TS for CO loss should dominate the competition.) Perhaps more significantly, the data can be reproduced over a wider energy range (by about 1 eV) when

the tighter $TS[N_1-O_3]$-ttgct ($\Delta S^{\ddagger}=-24$ J/K mol) is used compared with the looser $TS[O_1-O_3]$-ctggt ($\Delta S^{\ddagger}=-2$ J/K mol). (If these two TSs are given the same threshold energy, the rate for passing over the looser $TS[O_1-O_3]$ is ~10 times faster than for passing over $TS[N_1-O_3]$. Thus, TS $[O_1-O_3]$ for H_2O loss will dominate the competition if its threshold is lower, as suggested by B3LYP calculations (paper I). If the relative thresholds correspond to the MP2 result, i.e., $TS[N_1-O_3]$ is lower by 7 kJ/mol, the difference in rates drops to about a factor of two with $TS[O_1-O_3]$ still dominating. Thus, theory suggests that the data may be better interpreted in terms of $TS[O_1-O_3]$.) Thresholds for the H_2O and CO loss channels do not change appreciably (≤ 0.10 eV) no matter what combination of TSs are used. The largest change occurs for the $TS[O_1-O_3]$ / TS $[N_2]$-cggtt combination, where the tighter $TS[N_2]$-cggtt competing with the looser $TS[O_1-O_3]$ induces the largest competitive shift in the former threshold (as well as a poorer overall fit to the data).

The best reproduction of the data over the widest energy range is achieved by the $TS[N_1-O_3]$ / $TS[N_2]$-ttgtt combination of TSs and is shown in Figure 2a, but other combinations are nearly as accurate. The two cross sections are reproduced well over extended energy (from threshold up to ~4 eV, but only ~3 eV for $TS[O_1-O_3]$-ctggt) and magnitude ranges. This fidelity is particularly interesting given that the threshold for H_2O loss obtained from modeling is *lower* than that for CO loss by 0.07–0.19 eV, in contrast with the apparent relative thresholds observed. This properly reflects the fact that the TS for H_2O loss is much tighter ($\Delta S^{\ddagger}=-24$ or -2 J/K mol) than that for CO loss ($\Delta S^{\ddagger}=45$ or 50 J/K mol), such that the former channel has a larger kinetic shift in its threshold and a suppressed magnitude of its cross section. We also analyzed both cross sections independently (without competition), obtaining fitting parameters for CO loss that change little (Table 1) and suggesting a relatively small kinetic shift for this loose TS. For the H_2O loss channel, the thresholds increase by 0.02–0.10 eV, a rough measure of the kinetic shift; however, the shape of the cross section demands a much lower value of the parameter n, thereby forcing the threshold energy to higher values, which may prevent an effective measure of the kinetic shift in this case. Overall, the fact that both channels are accurately reproduced when using the competitive model despite the significant difference in the shapes of the cross sections lends support to the efficacy of the competitive statistical model in this system.

We also analyzed the competition between H_2O and CO loss assuming that H_2O loss leads to the protonated diketopiperazine species, H^+DKP, rather than the oxazolone. For this purpose, we used the lowest energy TS found in paper I leading to H^+DKP, $TS[N_1-O_3]$-ccctgc. Comparable fits to the data were obtained using this TS with a threshold for H_2O loss about 0.06 eV lower than that obtained for TS $[N_1-O_3]$-ttgct leading to H^+AMOx. This is because this TS is

tighter ($\Delta S^{\ddagger}=-39$ J/K mol) resulting in a larger kinetic shift. No change to the threshold for CO loss was observed compared with the models above.

Analysis of Cross Sections for H^+GG Decomposition—Sequential Dissociation Channels

There are two plausible pathways for reaction 7, loss of H_2O+CO: (a) H^+AMOx (b_2) + H_2O is formed via $TS[N_1-O_3]$ or $TS[O_1-O_3]$ as discussed above and then it sequentially decomposes by CO loss over $TS(H^+AMOx[N_2]$-c$\{OC\sim O\})$, Figure 4 of paper I, or (b) the $H^+AMOx(H_2O)$ complex is formed via these TSs and then it decomposes by losing CO over $TS(H^+AMOx[N_2]$-c$\{OC\sim O\})(H_2O_{HN2})$ followed by H_2O loss, Figure 4 of paper I. These calculations indicate that rate-limiting steps for these two pathways have energies of 225–230 and 180–194 kJ/mol, respectively. Figure 1 shows that the approximate threshold energy for reaction 7 is more consistent with the former. The failure to observe the lower energy pathway can be understood from the reaction coordinate surface in Figure 4 of paper I. This shows that once $H^+AMOx(H_2O)$ is formed, the tight $TS(H^+AMOx[N_2]$-c$\{OC\sim O\})(H_2O_{HN2})$ competes with loss of water, which is much lower in energy and involves a loose TS. Calculations of the rate coefficients for this competition demonstrate that the probability of reaching this tight TS is more than four orders of magnitude less probable than H_2O loss over the energy range examined experimentally. Thus, the cross section for reaction 7 was modeled as a sequential loss of H_2O (using either $TS[N_1-O_3]$ or $TS[O_1-O_3]$) followed by CO loss ($b_2 \rightarrow a_2$), while still modeling competition with the CO loss channels, the sum of reactions 5, 6, 8, and 9a, 9b, using $TS[N_2]$-ttgtt. The results of this sequential model using TS $[N_1-O_3]$ are shown in Figure 2b with optimized parameters for reaction 7 listed in Table 1. Thresholds for reactions 4 and 5 do not change. It can be seen that the model accurately reproduces all three channels over extended magnitude and energy ranges.

A similar approach was used to determine the thresholds for reaction 8 forming H^+G (y_1), the dominant decomposition product once CO is lost, Figure 1, as well as for reaction 9a forming $CH_2NH_2^+$ (a_1), and sequential loss of NH_3 in reaction 6. Specifically, these cross sections are modeled as H_2O loss (the sum of reactions 4 and 7 using either $TS[N_1-O_3]$ or $TS[O_1-O_3]$) competing with loss of CO (using $TS[N_2]$-ttgtt$\{C_{\alpha 1}\sim OC\sim N_2\}$) followed by competition between the sequential dissociation channels: CH_2NH and G loss over loose PSL TSs in reactions 8 and 9a (as in Figure 1 of paper I), and NH_3 loss over the tight $TS(C_3H_9N_2O_2^+[N_2-N_1]$-$(g_+t)gtt)$ (as in Figure 5 of paper I). (Three alternative TSs for NH_3 loss were also tried in the analysis, but these all gave very similar threshold energies for the five channels, most within 0.01 eV and all within 0.02 eV.) Significantly, the characteristics of the theoretical rate-limiting TSs (tight
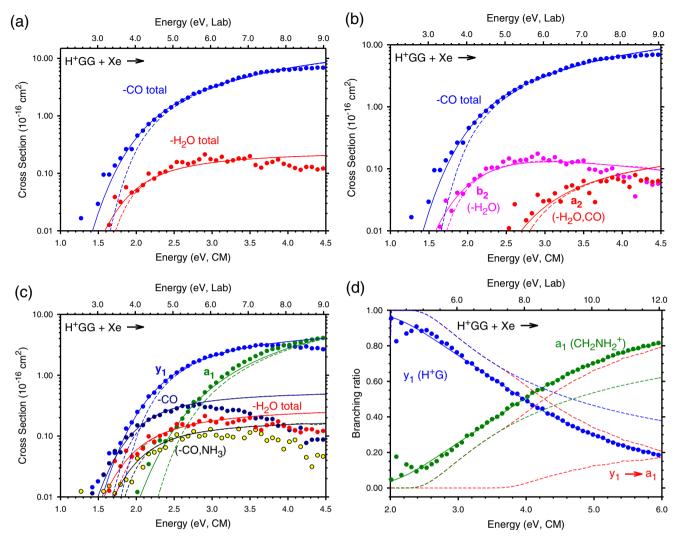
Figure 2. In all parts, symbols show data for the indicated process as a function of collision energy between H^+GG and Xe in the center-of-mass frame (lower x-axis) and the laboratory frame (upper x-axis). Solid lines show the best fit to the data using the models of Equation 1 and Equation 3 convoluted over the neutral and ion kinetic and internal energy distributions. Dashed lines show the model cross sections in the absence of experimental kinetic energy broadening for reactions with an internal energy of 0 K. (**a**) Modeling of composite cross sections for CO loss and H_2O loss from H^+GG. (**b**) Modeling of sequential decomposition of the H_2O loss product shown in part a, where the initially formed b_2 ion goes on to lose CO, in competition with the composite cross section for CO loss. (**c**) Modeling of sequential decomposition of the $(CH_2NH_2^+)G$ product formed by CO loss, where the initially formed ion goes on to form y_1 (H^+G), $a_1(CH_2NH_2^+)$, and to lose NH_3, in competition with the composite cross section for H_2O loss. (**d**) Branching fractions for the decomposition of the $(CH_2NH_2^+)G$ product formed by CO loss to y_1 (H^+G) and $a_1(CH_2NH_2^+)$. Contributions from the sequential decomposition of $y_1(H^+G)$ to $a_1(CH_2NH_2^+)$ are shown by the red curves

for reactions 4, 5, and 6 and loose for reactions 8 and 9a, 9b) are consistent with the relative magnitudes and energy dependences of the cross sections for these five channels, Figure 1. This model is generally insensitive to whether $TS[N_1\text{-}O_3]$ or $TS[O_1\text{-}O_3]$ is assumed for the H_2O loss channel, yielding thresholds for reactions 5, 6, 8, and 9a that are the same within 0.01 eV; however, the threshold for reaction 4 does change by 0.10 eV, similar to the results obtained for the simpler approaches outlined above. Significantly, no scaling of individual channels was required, except that a substantial increase in the relative amount of reaction 9a was required. This

result suggests that the competition between reactions 8 ($H^+G + CH_2NH$) and 9a ($CH_2NH_2^+ + G$) favors the latter products. This is potentially consistent with the quantum chemical results, which indicate that the initial complex formed after passing over the rate-limiting TS for loss of CO is $(OC_C)(CH_2NH_2^+)(G_{NH\cdot OC,CH\cdot N})$ (see Figure 1 in paper I), in which the proton is shared between the CH_2NH fragment and the carbonyl of glycine. Thus, this complex can decompose directly to $CH_2NH_2^+ + G + CO$, whereas formation of $H^+G + CH_2NH + CO$ with H^+G in its N protonated ground state conformation requires rearrangement to $(OC_{HN})(CH_2NH_2^+)(G_{NH\cdot N,CH\cdot OC})$ in which the

Table 1. Fitting parameters of Equation 1, threshold energies at 0 K, and entropies of activation at 1000 K[a]

Reaction		Transition state[b]	Competition[c]	σ_0	n	E_0 eV	$\Delta S_{1000}^{\ddagger}$ J / K mol
4	b_2 (H_2O Loss)	$[N_1\text{-}O_3]$	none	1.1 (0.9)	0.2 (0.1)	1.53 (0.07)	−24 (1)
			$[N_2]$-ttgtt	6.9 (1.1)	1.8 (0.1)	1.43 (0.05)	−24 (1)
			+seq	7.2 (1.0)	1.8 (0.1)	1.43 (0.05)	−24 (1)
			$[N_2]$-cggtt	7.5 (1.2)	1.7 (0.1)	1.45 (0.05)	−24 (1)
		$[O_1\text{-}O_3]$	none	0.5 (0.3)	0.7 (0.3)	1.51 (0.10)	−2 (1)
			$[N_2]$-ttgtt	6.8 (0.8)	1.8 (0.2)	1.49 (0.05)	−2 (1)
			+seq	7.4 (1.3)	1.7 (0.2)	1.53 (0.06)	−2 (1)
			$[N_2]$-cggtt	5.5 (1.2)	2.0 (0.2)	1.45 (0.06)	−2 (1)
		$H^+DKP[N_1\text{-}O_3]$	$[N_2]$-ttgtt	7.0 (1.1)	1.8 (0.2)	1.36 (0.05)	−39 (1)
5	CO Loss	$[N_2]$-ttgtt	none	6.2 (1.2)	1.9 (0.2)	1.60 (0.05)	50 (1)
			$[N_1\text{-}O_3]$	6.9 (1.1)	1.8 (0.1)	1.62 (0.05)	50 (1)
			+seq	7.2 (1.0)	1.8 (0.1)	1.63 (0.05)	50 (1)
			$[O_1\text{-}O_3]$	6.8 (0.8)	1.8 (0.1)	1.59 (0.05)	50 (1)
			+seq	7.4 (1.3)	1.7 (0.2)	1.64 (0.06)	50 (1)
		$[N_2]$-cggtt	none	6.4 (1.2)	1.8 (0.2)	1.58 (0.05)	45 (1)
			$[N_1\text{-}O_3]$	7.5 (1.2)	1.7 (0.1)	1.62 (0.05)	45 (1)
			$[O_1\text{-}O_3]$	5.5 (1.2)	2.0 (0.2)	1.52 (0.06)	45 (1)
7	a_2 (H_2O + CO loss)	$[N_1\text{-}O_3]{\rightarrow}H^+AMOx\{OC{\sim}O\}$	$[N_2]$-ttgtt	51 (14)	1.8 (0.1)	2.44 (0.13)	−53 (5)
		$[O_1\text{-}O_3]{\rightarrow}H^+AMOx\{OC{\sim}O\}$	$[N_2]$-ttgtt	11.2 (4.6)	2.0 (0.3)	2.37 (0.16)	−53 (5)
6	$C_3H_6NO_2^+$ + CO + NH_3	$[N_2]$-ttgtt${\rightarrow}NH_3$(TTS) + y_1(PSL) + a_1(PSL)	$[N_1\text{-}O_3]$	7.2 (1.0)	1.8 (0.1)	1.92 (0.07)	−50 (1)
			$[O_1\text{-}O_3]$	7.4 (1.3)	1.7 (0.2)	1.92 (0.07)	−50 (1)
8	$y_1(H^+G)$ + CH_2NH + CO	$[N_2]$-ttgtt${\rightarrow}$ y_1(PSL) + a_1(PSL) + NH_3 (TTS)	$[N_1\text{-}O_3]$	7.2 (1.0)	1.8 (0.1)	1.98 (0.07)	44 (5)
			$[O_1\text{-}O_3]$	7.4 (1.3)	1.7 (0.2)	1.99 (0.08)	44 (5)
9a	$a_1(CH_2NH_2^+)$ + G + CO	$[N_2]$-ttgtt${\rightarrow}a_1$(PSL) + y_1(PSL) + NH_3 (TTS)	$[N_1\text{-}O_3]$	290 (148)	1.8 (0.1)	2.19 (0.06)	52 (5)
			$[O_1\text{-}O_3]$	197 (123)	1.7 (0.2)	2.19 (0.07)	52 (5)
9b	$a_1(CH_2NH_2^+)$ + 2CO + CH_2NH + H_2O	$y_1{\rightarrow}H^+G[N\text{-}O_2]$-ct		35 (13)	1.8 (0.1)	3.36 (0.08)	36 (1)
		$y_1{\rightarrow}a_1$(PSL)		33 (12)	1.8 (0.1)	3.42 (0.09)	225 (5)

[a]Uncertainties in parentheses.
[b]$[N_1\text{-}O_3]$=TS$[N_1\text{-}O_3]$-ttgct. $[O_1\text{-}O_3]$=TS$[O_1\text{-}O_3]$-ctggt. $H^+DKP[N_1\text{-}O_3]$=TS$[N_1\text{-}O_3]$-ccctgc → H^+DKP. $[N_2]$-ttgtt=TS$[N_2]$-ttgtt$\{C_{\alpha 1}{\sim}OC{\sim}N_2\}$. $[N_2]$-cggtt= TS$[N_2]$-cggtt$\{C_{\alpha 1}{\sim}OC{\sim}N_2\}$. $H^+AMOx\{OC{\sim}O\}$=TS($H^+AMOx[N_2]$-c$\{OC{\sim}O\}$). NH_3(TTS)=$C_3H_9N_2O_2^+[N_2\text{-}N_1]$-(g$_+$t)gtt. PSL=loose phase space limit. An arrow indicates a sequential process with the indicated TSs for the initial and sequential steps.
[c]Competition with the indicated TSs is included in the modeling. + seq indicates that the analysis includes the sequential reactions 6, 8, and 9a.

proton is shared between the nitrogen atoms of the two fragments. Thus, even though reaction 8 is lower in energy, the requirement that the intermediate complex formed must rearrange for reaction 8 but not reaction 9a appears to enhance the probability of the latter reaction.

The results of this sequential-competitive model using TS $[N_1\text{-}O_3]$ are shown in Figure 2c with optimized parameters listed in Table 1. Thresholds for reactions (4) and (5) are the same as those for the simpler models within 0.05 eV, indicating that the introduction of the sequential channels does not greatly influence the overall energetics for the initial decomposition pathways. The model accurately reproduces all five channels over extended magnitude and energy ranges. The failure to reproduce the cross sections for the three reactions limited by tight TSs, reactions 4, 5, and 6, at the highest energies (above 3–3.5 eV) suggests that additional channels not considered begin to compete with these processes at higher energies or possibly that the statistical model may overestimate how much energy is carried away by the CO and H_2O.

It might be noted that we also tried modeling the competition between reactions 6, 8, and 9a as the competitive dissociation of the $(CH_2NH_2^+)(G_{NH{\bullet}N,CH{\bullet}OC})$ complex formed by CO loss from H^+GG, again using loose PSL TSs for

reactions 8 and 9a and a tight TS for reaction 6. This approach requires making additional assumptions about the energy available to the $(CH_2NH_2^+)(G)$ energized molecule. Nevertheless, similar threshold energies as those listed in Table 1 were obtained for formation of the y_1 and a_1 product ions, suggesting that the details of the modeling do not greatly affect the final thermodynamic results for the channels involving loose TSs. In contrast, reproduction of the cross section for loss of CO+NH_3 using this approach required a much lower energy threshold (11–33 kJ/mol lower than the computational predictions of paper I). This is believed to be because such a tight TS is affected much more strongly by the assumptions made regarding the energy and angular momentum retained by the $(CH_2NH_2^+)(G)$ complex.

Analysis of Cross Sections for H^+GG Decomposition—Third-Order Dissociation Channel

It is also possible to model reaction 9b, the sequential dissociation of the y_1 product ion to a_1. The cross section for this reaction is not appreciable until relatively high energies (above 4 eV), where our modeling no longer reproduces the

shape of the total cross section accurately, Figure 2a and b. However, the branching ratio between the y_1 and a_1 products can be modeled over a more extensive energy range using a combination of competition between reactions 8 and 9a (as described above) along with the sequential dissociation of reaction 9b ($y_1 \rightarrow a_1$). (The combined loss of $CO+NH_3$ in reaction 6 can also be included in this competition; however, because this channel involves a tight TS compared with the loose TSs for reactions 8 and 9a, its presence or absence does not affect the results.) The reaction coordinate surface for this subsequent dissociation has been discussed in detail in previous work and is limited by a tight TS, $H^+G([N-O_2]-$ ct), although some levels of theory find that the energy of the products lies slightly above this tight TS, such that a PSL TS may also be appropriate [10]. Results obtained assuming the tight TS for reaction 9b are shown in Figure 2d, where the deviation between experimental and predicted branching ratios resulting from the sequential dissociation is evident and can be easily modeled with the sequential dissociation model of Equation 3. Similar results are obtained assuming the PSL TS for reaction 9b. The optimized parameters obtained are listed in Table 1, where it can be seen that the threshold for reaction 9b is not very sensitive to which TS is assumed.

Discussion

In the study of Klassen and Kebarle (KK) [2], the cross sections for the y_1 and a_1 channels were modeled independently and only the model for the a_1 channel included consideration of kinetic shifts. They obtained a threshold
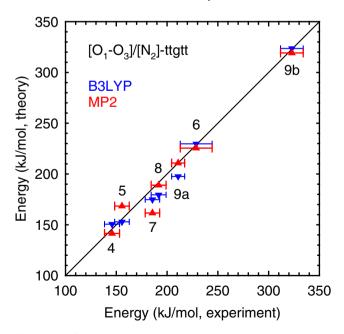
of 1.89 ± 0.26 eV for formation of a_1 (2.81 eV without kinetic shifts) and 2.35 eV for y_1 (not including kinetic shifts). The former value can be compared with the 2.19 ± 0.07 eV threshold we obtain for this product ion, Table 1. The difference is mainly attributable to the use of a tight TS by KK for this channel leading to a larger kinetic shift, in contrast to the loose PSL TS utilized here on the basis of the reaction coordinate diagram in Figure 1 of paper I. The failure to consider effects of competition between channels will also affect the comparison. The threshold for the y_1 ion obtained by KK is difficult to compare with the present results because it does not include consideration of kinetic shifts or competition. In the absence of kinetic shifts, KK find that the threshold for y_1 lies 0.46 eV below that for a_1, whereas we find a difference in the thresholds of about 0.2 eV. The effects of competition will reduce the threshold difference, as found here. Overall, given the complexity of the data analysis and the considerable effects of competition among the various channels (most of which were not observed by KK), the thresholds reported here for these reactions constitute the most reliable experimental gas-phase measurements.

It can be seen in Figure 2 that the experimental cross sections for reactions 4–9a, 9b are all reproduced well by Equations 1 and 3a, 3b over a large range of energies (almost 3 eV) and magnitudes (over two orders of magnitude). Comparison of the experimental threshold energies extracted from this modeling with 0 K values calculated at the B3LYP and MP2(full)/6-311+(2d,2p)// B3LYP/6-311+G(d,p) levels of theory for the rate-limiting TSs is provided in Table 2. Average experimental values adjusted to free energies at 298 K can be found in Table S1 of the Supplementary Material. Examination of these results shows that loss of H_2O unambiguously leads to the H^+AMOx product, rather than H^+DKP where theory and experiment disagree by over 110 kJ/mol. Excluding the H^+DKP pathway, it can be seen that the agreement between theory and experiment for all seven reactions is quite reasonable, as shown graphically in Figure 3 for the results obtained assuming TS $[O_1-O_3]$-ctggt for H_2O loss and TS$[N_2]$-ttgtt$\{C_{\alpha1}\sim OC\sim N_2\}$ for CO loss. One of the theoretical values generally falls within the range of uncertainty of our experimentally determined thresholds with the exception of $(CO+NH_3)$ loss, where theory falls just outside of the experimental uncertainty. For the latter channel, it is possible that the four TSs identified computationally, all TS$(C_3H_9N_2O_2^+[N_2-N_1])$ with different backbone conformations, are contributing to the observed reactivity, such that the measured threshold is an average of these TSs weighted by the rates of reactivity (which were determined above to be similar to each other). The energies of these four TSs vary from 174 to 186 kJ/mol (B3LYP) and 162 to 179 kJ/mol (MP2) with averages of 180 (B3LYP) and 171 (MP2) kJ/mol, compared with the measured threshold of 185 ± 7 kJ/mol. This kind of averaging among parallel TSs is also possible for all other pathways as well, but for these channels, alternative TSs are either similar in energy (and

Figure 3. Comparison of experimental threshold energies modeled using TS$[O_1-O_3]$-ctggt and TS$[N_2]$-ttgtt with B3LYP (blue inverted triangles) and MP2 (red triangles) single point energies taken from Table 2. Numbers refer to reactions 4–9a, 9b

Table 2. Comparison of Experimental and Theoretical Reaction Energies at 0 K for Decomposition of H^+GG (kJ/mol)

Reaction	Transition state[a]	Experiment[b]		Theory[c]	
		[N$_1$-O$_3$]	[O$_1$-O$_3$]	B3LYP	MP2
b$_2$ (H$^+$AMOx + H$_2$O)	[N$_1$-O$_3$] / [N$_2$]-ttgtt / [N$_2$]-cggtt	138 (5) 140 (5)		155	135
	[O$_1$-O$_3$] / [N$_2$]-ttgtt / [N$_2$]-cggtt		146 (7) 140 (6)	151	141
b$_2$ (H$^+$DKP + H$_2$O)	[N$_1$-O$_3$] / [N$_2$]-ttgtt	132 (5)		251	244
CO loss	[N$_2$]-ttgtt	157 (7)	156 (7)	153	168
	[N$_2$]-cggtt	156 (5)	146 (6)	154	168
a$_2$ (H$_2$O + CO loss)	b$_2$→H$^+$AMOx{OC~O}	236 (13)	229 (16)	230	226
C$_3$H$_6$NO$_2^+$ + CO+NH$_3$	[N$_2$]-ttgtt→NH$_3$-(g$_+$t)gtt	185 (7)	186 (7)	175	162
y$_1$(H$^+$G)+CO+CH$_2$NH	[N$_2$]-ttgtt→y$_1$(PSL)	191 (7)	192 (7)	180	189
a$_1$(CH$_2$NH$_2^+$)+CO+G	[N$_2$]-ttgtt→a$_1$(PSL)	212 (6)	211 (6)	198	211
a$_1$(CH$_2$NH$_2^+$)+H$_2$O+2CO+CH$_2$NH	y$_1$→H$^+$G([N-O$_2$]-ct)	323 (11)	323 (11)	324	319
	y$_1$→a$_1$(PSL)	329 (13)	329 (13)	316	326
MAD[d] (B3LYP)		9 (6)	8 (5)		
MAD[d] (MP2)		8 (7)	8 (9)		

[a][N$_2$]-ttgtt = TS[N$_2$]-ttgtt{C$_{\alpha 1}$~OC~N$_2$}. [N$_2$]-cggtt=TS[N$_2$]-cggtt{C$_{\alpha 1}$~OC~N$_2$}. [N$_1$-O$_3$]=TS[N$_1$-O$_3$]-ttgct. [O$_1$-O$_3$]=TS[O$_1$-O$_3$]-ctggt. (H$^+$AMOx){OC~O}=TS (H$^+$AMOx[N$_2$]-c {OC~O}). NH$_3$-(g$_+$t)gtt/g(gt)tc/tgtt/gttt=TS(C$_3$H$_9$N$_2$O$_2^+$[N$_2$-N$_1$]-(g$_+$t)gtt/-g(gt)tc/-tgtt/-gttt). PSL=loose phase space limit. An arrow indicates a sequential process with the indicated TSs for the initial and sequential steps.
[b]Experimental values from Table 1 with uncertainties in parentheses including values from competition with two possible rate-limiting TSs for H$_2$O loss, TS [N$_1$-O$_3$]-ttgct and TS[O$_1$-O$_3$]-ctggt.
[c]Computational results from Tables S1 and S2 of paper I [11].
[d]Mean absolute deviation from theoretical values, excluding results for H$^+$DKP + H$_2$O formation.

therefore explicitly considered in the results of Tables 1 and 2) or sufficiently high-lying that their rates are too slow for them to contribute substantially. Nevertheless, such considerations are probably useful to keep in mind whenever comparisons between experimental thresholds and the energies of specific TSs are made.

Overall, agreement between experiment and theory has a mean absolute deviation (MAD) of about 8 kJ/mol when comparing to the lowest energy TS for (CO+NH$_3$) loss. (The MADs decrease by about 1 kJ/mol if the average TS energy for NH$_3$ loss is used in comparison and by 2 kJ/mol if the (CO+NH$_3$) channel is excluded from the MP2 results). Comparable agreement is obtained for both B3LYP and MP2 theory and for the assumption that loss of H$_2$O occurs over TS[N$_1$-O$_3$]-ttgct versus TS[O$_1$-O$_3$]-ctggt. Similarly, good comparisons between experiment and theory with deviations near 10 kJ/mol have also been obtained previously for our studies of H$^+$G and H$^+$Asn fragmentations [10, 40]. The overall good agreement indicates that the rate-limiting TSs found computationally correct identify the mechanisms for all seven reactions investigated here.

We can also compare the energy measured here for subsequent decomposition of H$^+$G in reaction 9b with that measured in our laboratory previously for the direct dissociation of H$^+$G [10]. Here, we measure a threshold that is 133 ± 7 kJ/mol above that for formation of y$_1$ (139 ± 9 kJ/mol if the loose PSL TS is assumed). In our previous work, we measured that decomposition of H$^+$G over the tight TS [N-O$_2$]-ct requires 160 ± 5 kJ/mol, but that formation of the CH$_2$NH$_2^+$ + CO+H$_2$O products lie 140 ± 8 kJ/mol above H$^+$G. The latter value also agrees with literature thermochemistry that places the difference between the H$^+$G reactants and products

at 139.0 ± 8.2 kJ/mol [10]. In addition, the same level of theory used in paper I predicts that the tight TS lies at 132–144 kJ/mol, with the product energy at 137 kJ/mol. Thus, the threshold measured here matches the thermodynamic difference measured experimentally between H$^+$G and CH$_2$NH$_2^+$ + CO+H$_2$O rather than the energy measured for the rate-limiting TS. Within experimental error, it agrees with both quantities according to theory. The experimental discrepancy could indicate that decomposition of the H$^+$G fragment ion in the present system can occur more efficiently before the CO and CH$_2$NH neutral products have left, thereby lowering the barrier for H$^+$G fragmentation. It is also possible that the true energy of the tight TS[N-O$_2$]-ct is somewhat lower than measured in the H$^+$G system.

Conclusion

The kinetic energy dependence of the collision-induced dissociation of H$^+$GG with Xe is examined in a guided ion beam mass spectrometer. The threshold energies at 0 K for the sequential losses of H$_2$O+CO and CO+NH$_3$ as well as y$_1$ and a$_1$ ion formation are determined after consideration of the effects of reactant internal energy, multiple collisions with Xe, and lifetime effects [26, 37, 38]. The experimental results are compared with detailed quantum chemical calculations. Values are generally in reasonable agreement with calculations using the B3LYP and MP2(full)/6-311+(2d,2p)// B3LYP/6-311+G(d,p) levels of theory and are consistent with available computational characterizations in the literature. The thresholds reported here for these reactions constitute the first experimental gas-phase measurement of these reactions. The experimental results supported by theoretical calculations permit a systematic evaluation of the precise series of

molecular rotations and translocations that must be undergone in the reactions, including identification of the rate-limiting transition states, which dictate the threshold energies for the various processes. In accord with the general appearance of the data in Figure 1, formation of the y_1 and a_1 ions in reactions 8 and 9 are limited by loose PSL TSs, whereas the other four reactions involve passing over tight TSs, as identified in paper I.

It is noteworthy that the good agreement between the experimental and theoretical energetics generally allows an assignment of the structures formed at threshold in such systems. For instance, we can unambiguously assign the structure of the b_2 ion formed by dehydration in reaction 4 as protonated 2-aminomethyl-5-oxazolone (H^+AMOx), rather than protonated diketopiperazine (H^+DKP). The structures of $C_3H_9N_2O_2^+$ and the y_1 ion formed in reactions 5 and 8 are almost certainly $(CH_2NH_2^+)(G)$ and H^+G, although a range of possible conformations may be formed in the former case. At threshold, the $C_3H_7N_2O^+$ (a_2) product is likely to have the acyclic form (see Scheme 1), rather than the more stable cyclic form, a species that requires passing over a tight TS lying another 8–12 kJ/mol higher in energy according to theory [11]. In this regard, such structural identifications are comparable to those conducted by infrared multiple photon dissociation (IRMPD) experiments, in which comparison of the experimental spectra with theoretically calculated one-photon spectra often allow assignment of the structure. The advantage of the present approach is that the structural identification comes with equally useful thermodynamic information.

The good agreement between experiment and theory for the energetics of H^+GG decomposition indicates that our experiments begin with the ground state conformation, or only those conformations populated within a thermal equilibrium of the GS. (The distribution of conformations calculated for a thermal equilibrium using B3LYP/6-311+G(d,p), B3LYP/6-311+G(2d,2p), and MP2 (full)/6-311+G(2d,2p) free energies at 298 K indicates that the populations are 62%–78% $[N_1]$-ttttt, 4%–29% $[O_{1c}]$-ttttt, 2%–16% $[N_1]$-ttgtt, 0.3%–3% $[O_{1t}]$-ctctt, and less than 1% for all other conformers. See paper I for a description of these conformers.) The multitude of products observed does not require a large distribution of conformations formed in the source. Because the observed decompositions clearly require movement of the extra proton, as elucidated in the reaction coordinate surfaces shown in paper I, the present results show that the proton is mobile once the ground state is collisionally excited, at least on a scale of hundreds of μs. As such, these results provide a detailed look at the facility of the "mobile proton" [12], and hopefully provide insight into the detailed mechanisms associated with the fragmentation of protonated proteins. The ability to accurately predict the energetics of such fragmentations also portends well for ultimately being able to quantita-tively predict the resultant mass spectra, perhaps increasing the facility, reliability, and completeness of sequence identification.

Acknowledgment

References

1. Tsang, C.W., Harrison, A.G.: Chemical ionization of amino acids. *J. Am. Chem. Soc.* **98**, 1301–1308 (1976)
2. Klassen, J.S., Kebarle, P.: Collision-induced dissociation threshold energies of protonated glycine, glycinamide, and some related small peptides and peptide amino amides. *J. Am. Chem. Soc.* **119**, 6552–6563 (1997)
3. El Aribi, H., Rodriquez, C.F., Almeida, D.R.P., Ling, Y., Mak, W.W.-N., Hopkinson, A.C., Siu, K.W.M.: Elucidation of fragmentation mechanisms of protonated peptide ions and their products: a case study on glycylglycylglycine using density functional theory and threshold collision-induced dissociation. *J. Am. Chem. Soc.* **125**, 9229–9236 (2003)
4. Abirami, S., Xing, Y.M., Tsang, C.W., Ma, N.L.: Theoretical study of α/β-alanine and their protonated/alkali metal cationized complexes. *J. Phys. Chem. A* **109**, 500–506 (2005)
5. Laskin, J., Denisov, E., Futrell, J.: A comparative study of collision-induced and surface-induced dissociation. 1. Fragmentation of protonated dialanine. *J. Am. Chem. Soc.* **122**, 9703–9714 (2000)
6. Reid, G.E., Simpson, R.J., O'Hair, R.A.J.: A mass spectrometric and Ab initio study of the pathways for dehydration of simple glycine and cysteine-containing peptide [M+H]$^+$ ions. *J. Am. Soc. Mass Spectrom.* **9**, 945–956 (1998)
7. Reid, G.E., Simpson, R.J., O'Hair, R.A.J.: Probing the fragmentation reactions of protonated glycine oligomers via multistage mass spectrometry and gas phase ion molecule hydrogen/deuterium exchange. *Int. J. Mass Spectrom.* **190/191**, 209–230 (1999)
8. Pingitore, F., Polce, M.J., Wang, P., Wesdemiotis, C., Paizs, B.: Intramolecular condensation reactions in protonated dipeptides: carbon monoxide, water, and ammonia losses in competition. *J. Am. Soc. Mass Spectrom.* **15**, 1025–1038 (2004)
9. El Aribi, H., Orlova, G., Rodriquez, C.F., Almeida, D.R.P., Hopkinson, A.C., Siu, K.W.M.: Fragmentation mechanisms of product ions from protonated tripeptides. *J. Phys. Chem. B* **108**, 18743–18749 (2004)
10. Armentrout, P.B., Heaton, A.L., Ye, S.J.: Thermodynamics and mechanisms for decomposition of protonated glycine and its protonated dimer. *J. Phys. Chem. A*, in press (2011)
11. Armentrout, P.B., Heaton, A.L.: Thermodynamics and mechanisms of protonated diglycine decomposition: a computational study. *J. Am. Soc. Mass Spectrom.*, doi:10.1007/s13361-011-0224-7 (2011)
12. Dongre, A.R., Jones, J.L., Somogyi, A., Wysocki, V.H.: Influence of peptide composition, gas-phase basicity, and chemical modification on fragmentation efficiency: evidence for the mobile proton model. *J. Am. Chem. Soc.* **118**, 8365–8374 (1996)
13. Ervin, K.M., Armentrout, P.B.: Translational Energy Dependence of Ar$^+$ + XY → ArX$^+$ + Y (XY = H$_2$, D$_2$, HD) from Thermal to 30 eV c.m. *J. Chem. Phys.* **83**, 166–189 (1985)
14. Muntean, F., Armentrout, P.B.: Guided ion beam study of collision-induced dissociation dynamics: integral and differential cross sections. *J. Chem. Phys.* **115**, 1213–1228 (2001)
15. Moision, R.M., Armentrout, P.B.: An electrospray ionization source for thermochemical investigation with the guided ion beam mass spectrometer. *J. Am. Soc. Mass Spectrom.* **18**, 1124–1134 (2007)
16. Moision, R.M., Armentrout, P.B.: An experimental and theoretical dissection of sodium cation/glycine interactions. *J. Phys. Chem. A* **106**, 10350–10362 (2002)
17. Heaton, A.L., Moision, R.M., Armentrout, P.B.: Experimental and theoretical studies of sodium cation interactions with the acidic amino

acids and their amide derivatives. *J. Phys Chem. A* **112**, 3319–3327 (2008)

18. Heaton, A.L., Armentrout, P.B.: Experimental and theoretical studies of potassium cation interactions with the acidic amino acids and their amide derivatives. *J. Phys. Chem. B* **112**, 12056–12065 (2008)

19. Kim, T., Tolmachev, A.V., Harkewicz, R., Prior, D.C., Anderson, G., Udseth, H.R., Smith, R.D.: Design and implementation of a new electrodynamic ion funnel. *Anal. Chem.* **72**, 2247–2255 (2000)

20. Ye, S.J., Moision, R.M., Armentrout, P.B.: Sequential bond energies of water to sodium glycine cation. *Int. J. Mass Spectrom.* **240**, 233–248 (2005)

21. Teloy, E., Gerlich, D.: Integral cross sections for ion–molecule reactions. I. The guided beam technique. *Chem. Phys.* **4**, 417–427 (1974)

22. Gerlich, D.: Inhomogeneous rf fields: a versatile tool for the study of processes with slow ions. *Adv. Chem. Phys.* **82**, 1–176 (1992)

23. Aristov, N., Armentrout, P.B.: Collision induced dissociation of vanadium monoxide ion. *J. Phys. Chem.* **90**, 5135–5140 (1986)

24. Dalleska, N.F., Honma, K., Sunderlin, L.S., Armentrout, P.B.: Solvation of transition metal ions by water. sequential binding energies of $M^+(H_2O)x$ (x = 1–4) for M = Ti - Cu determined by collision-induced dissociation. *J. Am. Chem. Soc.* **116**, 3519–3528 (1994)

25. Daly, N.R.: Scintillation type mass spectrometer ion detector. *Rev. Sci. Instrum.* **31**, 264–267 (1960)

26. Rodgers, M.T., Armentrout, P.B.: Statistical modeling of competitive threshold collision-induced dissociation. *J. Chem. Phys.* **109**, 1787–1800 (1998)

27. Muntean, F., Armentrout, P.B.: Modeling kinetic shifts for tight transition states in threshold collision-induced dissociation. Case study: phenol cation. *J. Phys. Chem. B* **106**, 8117–8124 (2002)

28. Muntean, F., Heumann, L., Armentrout, P.B.: Modeling kinetic shifts in threshold collision-induced dissociation. Case study: dichlorobenzene cation dissociation. *J. Chem. Phys.* **116**, 5593–5602 (2002)

29. Muntean, F., Armentrout, P.B.: Modeling kinetic shifts and competition in threshold collision-induced dissociation. Case study: n-butylbenzene cation dissociation. *J. Phys. Chem. A* **107**, 7413–7422 (2003)

30. Narancic, S., Bach, A., Chen, P.: Simple fitting of energy-resolved reactive cross sections in threshold collision-induced dissociation (T-CID) experiments. *J. Phys. Chem. A* **111**, 7006–7013 (2007)

31. Jia, B., Angel, L.A., Ervin, K.M.: Threshold collision-induced dissociation of hydrogen-bonded dimers of carboxylic acids. *J. Phys. Chem. A* **112**, 1773–1782 (2008)

32. Gilbert, R.G., Smith, S.C.: Theory of Unimolecular and Recombination Reactions. Blackwell Scientific, London (1990)

33. Robinson, P.J., Holbrook, K.A.: Unimolecular Reactions. Wiley Interscience, New York (1972)

34. Beyer, T.S., Swinehart, D.F.: Algorithm 448: number of multiply-restricted partitions. *Commun. ACM* **16**, 379 (1973)

35. Stein, S.E., Rabinovitch, B.S.: Accurate evaluation of internal energy level sums and densities including anharmonic oscillators and hindered rotors. *J. Chem. Phys.* **58**, 2438–2445 (1973)

36. Stein, S.E., Rabinovitch, B.S.: On the use of exact state counting methods in RRKM rate calculations. *Chem. Phys. Lett.* **49**, 183–188 (1977)

37. Rodgers, M.T., Ervin, K.M., Armentrout, P.B.: Statistical modeling of collision-induced dissociation thresholds. *J. Chem. Phys.* **106**, 4499–4508 (1997)

38. Armentrout, P.B.: Statistical modeling of sequential collision-induced dissociation thresholds. *J. Chem. Phys.* **126**, 234–302 (2007)

39. Hales, D.A., Lian, L., Armentrout, P.B.: Collision-induced dissociation of Nb_n^+ (n=2–11): bond energies and dissociation pathways. *Int. J. Mass Spectrom. Ion Processes* **102**, 269–301 (1990)

40. Heaton, A.L., Armentrout, P.B.: Thermodynamics and mechanism of protonated asparagine decomposition. *J. Am. Soc. Mass Spectrom.* **20**, 852–866 (2009)